Gated and Near-Surface Diffusion of Charged Fullerenes in Nanochannels

Alessandro Grattoni,[†] Daniel Fine,[†] Erika Zabre,[†] Arturas Ziemys,[†] Jaskaran Gill,[†] Yuri Mackeyev,[‡] Matthew A. Cheney,[‡] Delia C. Danila,[§] Sharath Hosali,[⊥] Lon J. Wilson,[‡] Fazle Hussain,[†,∥] and Mauro Ferrari[†,#,*]

[†]Department of Nanomedicine, Methodist Hospital Research Institute, 6670 Bertner Street, M.S. R2-216, Houston, Texas 77030, United States, [‡]Department of Chemistry, Rice University, 6100 Main Street, Houston, Texas 77005, United States, [§]Department of Internal Medicine, University of Texas Health Science Center at Houston, 6431 Fannin Street, Houston, Texas 77030, United States, [⊥]NanoMedical Systems, Inc., 2706 Montopolis Drive, Austin, Texas 78741, United States, [∥]Departments of Mechanical Engineering, Physics, and Geosciences, University of Houston, N207 Engineering Building 1, Houston, Texas 77204, United States, and [#]Department of Bioengineering, Rice University, 6100 Main Street, Texas 77005, United States

ABSTRACT

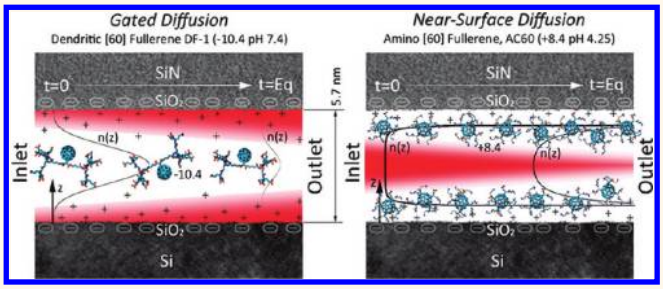

Nanoparticles and their derivatives have engendered significant recent interest. Despite considerable advances in nanofluidic physics, control over nanoparticle diffusive transport, requisite for a host of innovative applications, has yet to be demonstrated. In this study, we performed diffusion experiments for negatively and positively charged fullerene derivatives (dendritic fullerene-1, DF-1, and amino fullerene, AC60) in 5.7 and 13 nm silicon nanochannels in solutions with different ionic strengths. With DF-1, we demonstrated a *gated* diffusion whereby precise and reproducible control of the dynamics of the release profile was achieved by tuning the gradient of the ionic strength within the nanochannels. With AC60, we observed a *near-surface* diffusive transport that produced release rates that were independent of the size of the nanochannels within the range of our experiments. Finally, through theoretical analysis we were able to elucidate the relative importance of physical nanoconfinement, electrostatic interactions, and ionic strength heterogeneity with respect to these *gated* and *near-surface* diffusive transport phenomena. These results are significant for multiple applications, including the controlled administration of targeted nanovectors for therapeutics.

KEYWORDS: nanoconfinement · electrostatics · ionic strength · controlled delivery · nanocarriers · silicon membranes · [60]fullerene

Precise control over the fluidic transport of nanoparticles and biomolecules represents a fundamental requirement in the development of many innovative technologies that aim to exploit their unique properties.[1−3] In particular, the ability to tune nanoparticle diffusion dynamics yields new opportunities for the delivery of pharmaceuticals whereby nanoparticles can be engineered to carry both drugs and surface-functionalized targeting moieties.[4−7] Such a capability would also enable metronomic delivery whereby the timing of the delivery is as equally important as the amount administered.[8,9]

Recently, nanochannels have been employed for passively controlling the diffusive transport of a variety of clinically relevant molecules.[10] Despite the successful demonstration of zero-order release for a wide range of analytes presenting different sizes, morphologies, charge states, and surface residues,[11,12] as well as the important theoretical contributions from hindered transport theory,[13] a full description of the physics of nanoscale fluidic transport had yet to be achieved. The difficulty in providing such a description derives from the highly coupled effects of charge distribution, spatial confinement, and surface-to-molecule interactions present at the nanoscale, where surface properties begin to dominate over volume properties.[14−16] Many of these effects are primary contributors to concentration-independent transport and cannot be considered solely on the basis of adjustments to important diffusion and hydrodynamic parameters.

In this work, we have experimentally and theoretically studied the constrained diffusion of highly charged negative and positive fullerene nanoparticles (dendritic fullerene-1, DF-1, and amino fullerene, AC60) through nanochannels, constructs previously investigated as nanocarriers for therapeutics[17−22] and reliable and stable probes for diffusive transport of charged particles.[23] The measurements were carried out using UV spectroscopy at absorption wavelengths of 320 and 280 nm (for DF-1

* Address correspondence to mferrari@tmhs.org.

Received for review February 25, 2011 and accepted October 27, 2011.

Published online October 28, 2011
10.1021/nn2037863

TABLE 1. DF-1 and AC60 Source Solutions and Sink Fluids (at time $t = 0$) and Debye Lengths, λ_D, Calculated at Time $t = 0$ and $t = Eq$

fullerene	source solution (at $t = 0$)		sink fluid (at $t = 0$)	λ_D $t = 0$ [nm]	λ_D $t = Eq$ [nm]
DF-1	H_2O, 50 mM NaCl, 11 mM Na_2CO_3 (at pH 7.4)	(I_H)	H_2O, 50 mM NaCl	1.19	1.36
DF-1	H_2O, 11 mM Na_2CO_3 (at pH 7.4)	(I_L)	H_2O	2.38	13.19
AC60	H_2O, 50 mM NaCl, 2.86 mM $NaHCO_3$ (pH 4.25)	(I_H)	H_2O, 50 mM NaCl	0.98	1.04
AC60	H_2O, 2.86 mM $NaHCO_3$ (pH 4.25)	(I_L)	H_2O	1.41	1.95

and AC60, respectively) in a custom-designed diffusion apparatus described in Methods. First, we analyze the variation over time of the ionic strength of the solution and its effect on the electrical double layer (EDL) and dynamics of transport. We then investigate and elucidate the theoretical basis for the *gated* diffusive transport of negative DF-1 and the *near-surface* diffusion of positive AC60.

RESULTS AND DISCUSSION

Ionic Strength and Electrical Double Layer. The ionic strength (I) and the dielectric properties of fluids determine the size of the EDL adjacent to the negatively charged silica walls. To investigate the effect of different I's, and thus EDLs, on the diffusive transport of the oppositely charged fullerene derivatives in nanoconfinement, DF-1 and AC60 solutions with both low and high ionic strengths (I_L and I_H, respectively) were prepared and employed in release tests performed with dual-chamber UV-diffusion devices as described in the Methods and elsewhere.[24] Table 1 details the contents of the source and sink solutions used in the experiments. In addition, to evaluate the effect of the variation of I over time, we exploited the initial ionic strength imbalance created by the sodium carbonate and sodium bicarbonate that were added to the source solutions to stabilize DF-1 and AC60, respectively, by adjusting the pH to 7.4 (DF-1) and 4.25 (AC60). The natural short-term equilibration of the ionic concentration between the source and sink reservoirs allowed for the analysis of DF-1 and AC60 transport under transient conditions of varying ionic strength, without obscuring long-term diffusive behavior. The imbalance of DF-1, AC60, and other ions in the system also generates an osmotic potential, which is proportional to the differential concentration, Δc. However, the effect of the osmotic transport of solvent was neglected, Δc being small for all ions in solution.

The approximate thickness of the EDL, known as the Debye length (λ_D), increases with decreasing ionic strength, as fewer solvated ions are available to screen the SiO_2 surface charge. Table 1 lists λ_D values for both DF-1 and AC60 in the I_L and I_H solutions calculated as follows:[25]

$$\lambda_D = \sqrt{\frac{\varepsilon\varepsilon_0 k_B T}{e^2 \sum_i n_i z_i^2}} \quad (1)$$

where ε is the dielectric constant of the solvent, ε_0 is the dielectric permittivity of free space, k_B is Boltzmann's constant, T is the absolute temperature, e is the charge of an electron, and n_i and z_i are the concentration and the valence of the ith species, respectively. The relatively low concentrations of both AC60 and DF-1, as compared to the other ionic species, lead to an average minimum distance between particles, ℓ, of 10.8 and 11.6 nm, respectively, within the source solution (calculated as $N^{-1/3}$, where N is the number density at the maximum concentration of 3 mg/mL). The high positive valence of AC60 (+8.4 at pH 4.25), however, drives accumulation near the nanochannel wall's surface, which increases its concentration over the source solution (this will be elucidated later). AC60 is therefore likely to contribute globally to the EDL, despite its relatively large size sufficient to develop its own EDL, and so is included in the first-order calculation of λ_D. DF-1, with its high negative valence (−10.4e at pH 7.4), is generally repulsed from the nanochannel wall's surface, reducing its concentration with respect to the source and increasing its interparticle spacing over the already large value listed above. At these interparticle distances, DF-1 is deemed to produce only local perturbations to the nanochannel EDL during transit, without homogeneously and permanently contributing to a global variation, and is therefore excluded from the calculation of λ_D (see Supporting Information for additional details on the λ_D calculation). The time variation of I required the determination of λ_D at two distinct time points: (1) at $t = 0$, before the diffusion of any ionic species occurs; (2) At $t = Eq$, corresponding to the establishment of a quasi-equilibrium of the ionic species distributions (with the exception of DF-1 and AC60) between the source and sink reservoirs.

The values of λ_D depicted in Table 1 demonstrate that at higher ionic strength the EDLs that line the walls of both the 5.7 and 13 nm nanochannels do not overlap at any time, $t = 0$ or $t = Eq$. In the case of the lower ionic strength solutions, however, the EDLs significantly overlap in both the 5.7 and 13 nm nanochannels at $t = Eq$ after the ionic distribution (except DF-1 and AC60) has reached quasi-equilibrium. When the EDLs overlap, the nanochannel wall surface charge cannot be fully screened by the ionic species in solution, resulting in either a *gated* or a *near-surface*

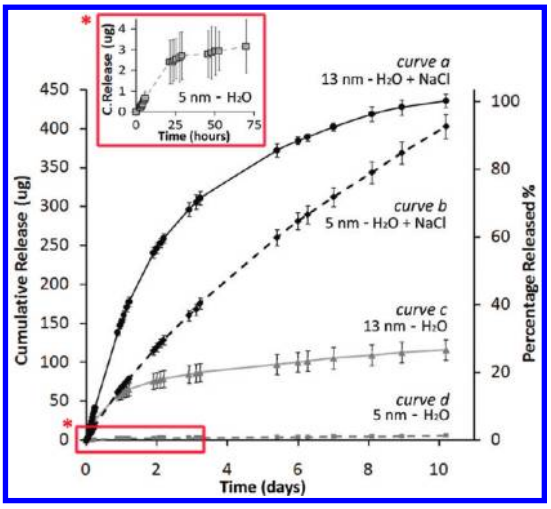

Figure 1. Cumulative released amount and percentage release of DF-1 in I_H and I_L solutions in 5.7 and 13 nm nanochannels.

accumulation effect for negative and positive charges, respectively, that approach the nanochannel inlet.

Gated Diffusion of Negatively Charged DF-1. The functionalized DF-1 (MW = 2827 Da) presents dimensions of approximately 3 × 2 × 1.5 nm (corresponding to the minimized structure in water), including its two dendritic arms, and has 18 carboxylic acid surface residues, leading to a net charge of −10.4*e* at pH 7.4.[26] When diffusing within a narrow nanochannel, DF-$1^{10.4-}$ experiences an electrostatic repulsion from the channel walls associated with the surface charge, which limits the cross section of the nanochannel that can be occupied by the charged DF-1 without significant energetic penalties (ΔG). Using a *z*-potential analyzer (Delsa Nano C, Beckman Coulter, Inc.) we measured a negative surface charge density associated with the silicon dioxide nanochannel walls of approximately $-1\ \mu C/cm^2$, a value that is consistent with the literature.[27]

For DF-1 in the I_H solution (see Table 1), the concentration of cationic charges (Na^+ and H_3O^+) is sufficient to shorten the EDL (minimize λ_D) at both $t = 0$ and $t = Eq$ such that DF-1 can diffuse through the nanochannel freely (in 13 nm) or with low energetic penalties related to the reduced translational degrees of freedom (in 5.7 nm). Similar results related to the connection between pH and the diffusion of lectin have been reported.[28] The release results shown in Figure 1 (curves *a* and *b*) clearly represent this effect, showing a seemingly unperturbed Fickian release profile of DF-1 nanoparticles in I_H solution in 13 nm and the characteristic quasi-linear release profile in 5.7 nm, similar to what has been observed in the literature for molecules diffusing under nanoconfined conditions.[23]

These high ionic strength effects are schematically represented in Figure 2A for the 13 nm nanochannels. In this case, only a modest variation in the electric potential profile $\psi(z)$, established by the negative surface charge and the EDL, occurs between $t = 0$ and $t = Eq$, which leads to a slight shrinking of the normalized number density profile $n(z)$ across the nanochannel cross section (normalized with respect to the source reservoir concentration).

When DF-1 is dissolved in the Na_2CO_3-buffered I_L solution (no NaCl added) and released into pure DI water, the ionic strength within the nanochannels decreases between $t = 0$ and $t = Eq$, as is evident by the change in release dynamics of curves *c* and *d* in Figure 1. At $t = 0$, the *I* is sufficiently high that the EDLs of the nanochannel walls do not occupy the entire nanochannel cross section and rapid release is observed. This ionic imbalance between the source and sink reservoirs, however, drives a net flux of all ions down their respective concentration gradients. The charged species in the source solution include DF-$1^{10.4-}$ and the dissociation products of the sodium carbonate buffer (Na^+, HCO_3^-, and CO_3^{2-}). The bulk diffusivities of Na^+ (1.3×10^{-5} cm^2/s), HCO_3^- (1.19×10^{-5} cm^2/s),[29] and CO_3^{2-} (0.92×10^{-5} cm^2/s)[30] are 1 to 4 orders of magnitude higher than for DF-$1^{10.4-}$ diffusing through the nanochannels (the DF-1 experimental diffusivity analysis is discussed later). In addition, the above low-valence ionic species are partially (HCO_3^-, CO_3^{2-}) or completely (Na^+) unaffected by the negative surface charge in the nanochannel, as compared to the DF-1.[31] As such, these smaller and less charged ions rapidly redistribute between the source and sink reservoirs, causing an increase in λ_D and a corresponding decrease of the effective nanochannel cross section that allows for low-energy loss of DF-1 occupancy.

At $t = Eq$, a quasi-equilibrium is reached in the source and sink reservoirs between the chemical and Nernst potentials arising from the charge concentration imbalances of Na^+, HCO_3^-, CO_3^{2-}, and the DF-1. By considering that the smaller ionic species equilibrate much more rapidly than DF-1, regardless of their positive or negative charge, $t = Eq$ was estimated by neglecting the effect of the Nernst potential buildup. The obtained $t = Eq$ values (0.9 and 1.7 days for 13 and 5.7 nm, respectively, in I_L solutions), corresponding to 95% of the equilibration, are in agreement with the experimental observation, approximating the time at which a steady-state release is established (see Figure 1 curves *c* and *d*). Details are available in the Supporting Information. The EDLs from the nanochannel walls and the DF-1 now overlap (see Table 1), with the resulting reduction in negative charge screening producing a significant energetic barrier, E_B, to the diffusion of DF-1^{32} through the nanochannels due to electrostatic repulsion. This dramatic increase in the potential barrier as the ionic strength shifts from high to low is graphically shown in Figure 2B for the 5.7 nm nanochannels. $\psi(z)$ flattens between $t = 0$ and $t = Eq$ such that the potential in the center of the nanochannel is close in magnitude to the wall potential and correspondingly

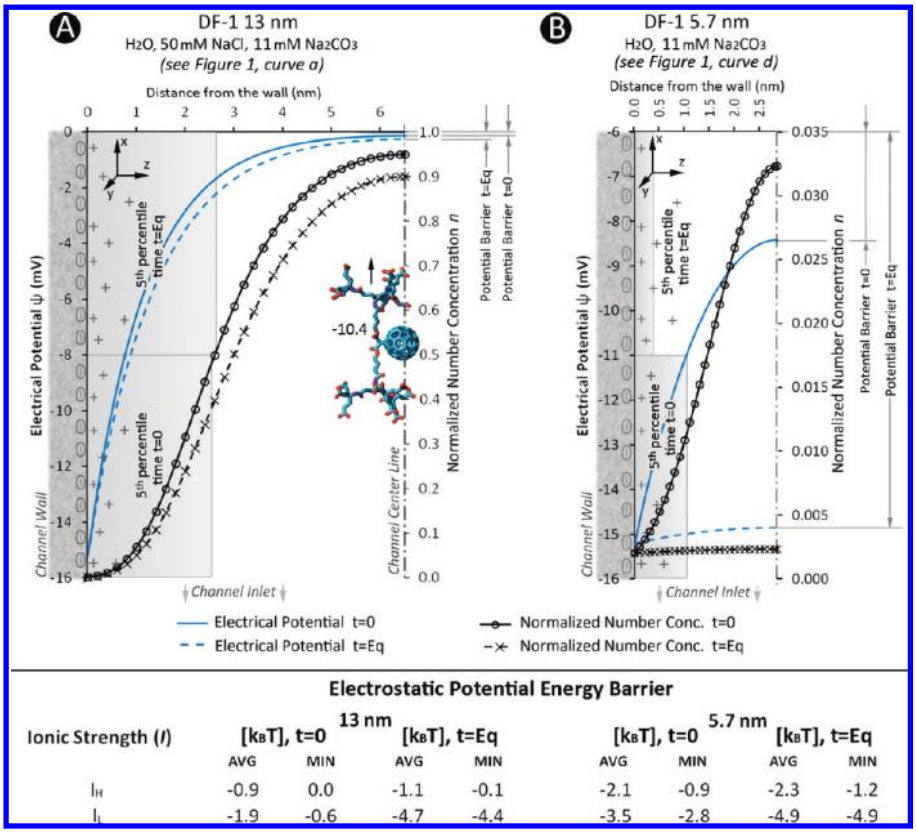

Electrostatic Potential Energy Barrier

Ionic Strength (*I*)	13 nm [k_BT], t=0 AVG	13 nm [k_BT], t=0 MIN	13 nm [k_BT], t=Eq AVG	13 nm [k_BT], t=Eq MIN	5.7 nm [k_BT], t=0 AVG	5.7 nm [k_BT], t=0 MIN	5.7 nm [k_BT], t=Eq AVG	5.7 nm [k_BT], t=Eq MIN
I_H	-0.9	0.0	-1.1	-0.1	-2.1	-0.9	-2.3	-1.2
I_L	-1.9	-0.6	-4.7	-4.4	-3.5	-2.8	-4.9	-4.9

Figure 2. Schematic representations of the electrical potential, $\psi(z)$, and number concentration, $n(z)$, profiles as well as the effective cross sections at times $t = 0$ and $t =$ Eq for DF-1 in I_H (A) and I_L (B) ionic strength solutions in both 13 (A) and 5.7 (B) nm nanochannels. For symmetry reasons, the panels show only half of the nanochannel cross section. The time $t =$ Eq represents the establishment of a quasi-equilibrium whereby the concentrations of all other ionic species (Na^+, Cl^-, HCO_3^-, and CO_3^{2-}) except the ionized DF-1 have reached a steady state between the source and sink solutions. $n(z)$ has been normalized with respect to the source solution concentration. The surface charge density on the nanochannel wall was measured to be -1 μC/cm^2. The depletion regions (lighter gray areas) represent the portion of the channel cross section that is occupied by the 5%ile of the $n(z)$ distribution at $t = 0$ and $t =$ Eq. The increase in the potential barrier at equilibration resulting from electrostatic repulsion of the ionized DF-1$^{10.4-}$ by the negative surface charge is also shown to the right side of each panel. The values of the electrostatic potential energy barrier, E_B, are listed in the table. The calculations for all values can be found in Methods and the Supporting Information.

leads to a significant reduction in the $n(z)$ peak height by over 2 orders of magnitude. The calculated values of the energy barriers for DF-1 diffusing through both nanochannel sizes in I_L and I_H solutions at $t = 0$ and $t =$ Eq can be found in the table in Figure 2 (see the Supporting Information for details on the calculation of E_B). The higher energy barriers lead to lower release rates because of fewer particles with sufficient thermal energy to surmount the potential energy barrier, as can been seen from a comparison of the release rates produced by the high and low ionic strength solutions calculated from Figure 1: 39.5 to 0.45 μg/day for 5.7 nm (a 98.4% reduction) and a rapid Fickian profile (450 μg over 10 days) to 4.3 μg/day for 13 nm. The zero-order release regions for buffered DF-1 into DI water follow exponential transients that exceed 21 and 52 h in the 5.7 and 13 nm nanochannels, respectively. To validate our hypothesis of an energy barrier mediated release, and to exclude the possibility of the change in release rate being caused by DF-1 aggregation, a diffusion experiment was performed during which DF-1 I_L source solutions were spiked with NaCl after the establishment of quasi-equilibrium. The observed immediate rise in release rate, with a slope proportional in magnitude to the DF-1 concentration gradient, indicates that the added salt causes a modulation in the barrier height as salt would normally facilitate aggregation by shielding negative charge (allowing closer particle-to-particle proximity; the experiment is detailed in the Supporting Information).[33]

To further investigate the role that ionic strength and electrostatic repulsion has on DF-1 diffusive transport through nanochannels, we calculated the effective diffusivity, D_{EXP}, of DF-1 by fitting the experimental data with the following exponential curve:[34]

$$m(t) = (c_{IN} - c_{OUT})\frac{V_{IN}V_{OUT}}{V_{IN} + V_{OUT}}(1 - e^{-\tau t}) \quad (2)$$

$$\tau = \left(\frac{D_{exp}}{R_{eq}V_{IN}}\right)\left(1 + \frac{V_{IN}}{V_{OUT}}\right) \quad (3)$$

where $m(t)$ is the mass released over time, c_{IN} and c_{OUT} are the concentrations of DF-1 in the source and sink

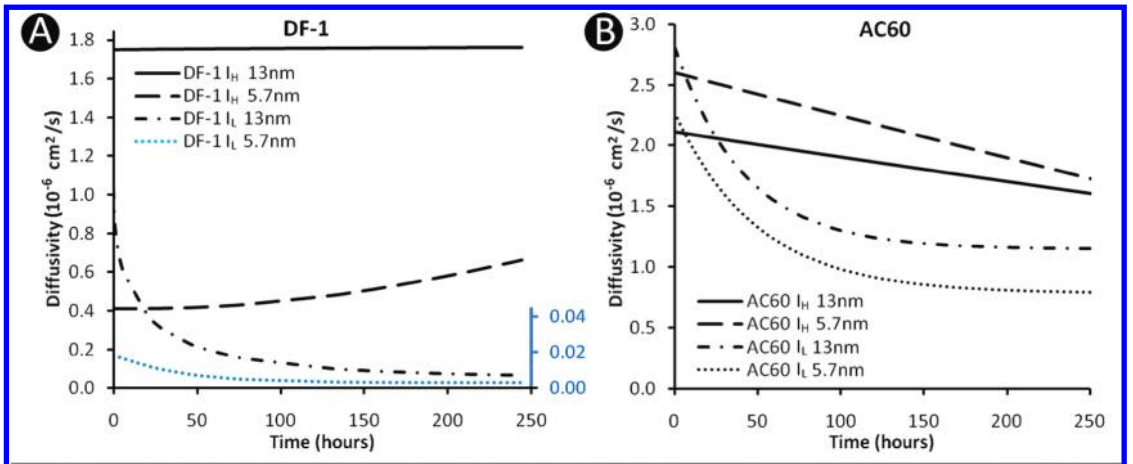

FULLERENE	Solution		Channel Size (nm)	Diffusivity (10^{-6} cm²/s) at 22.5±0.15°C t=0	t=End	R^2	AVG%DIFF
DF-1	H_2O, 50 mM NaCl, 11 mM Na_2CO_3	(IH)	3, 200 μm (Bulk)	1.75	1.75	0.999	0.9
			13	1.75	1.76	0.998	1.8
			5.7	0.41	0.66	0.999	1.0
DF-1	H_2O, 11 mM Na_2CO_3	(IL)	3, 200 μm (Bulk)	4.14	4.14	0.999	1.3
			13	1.03	0.07	0.999	1.0
			5.7	0.02	0.003	0.990	3.1
AC60	H_2O, 50 mM NaCl, 2.86 mM $NaHCO_3$	(IH)	3, 200 μm (Bulk)	2.61	2.61	1.000	0.7
			13	2.11	1.59	1.000	0.5
			5.7	2.6	1.69	0.999	1.0
AC60	H_2O, 2.86 mM $NaHCO_3$	(IL)	3, 200 μm (Bulk)	4.41	4.41	0.999	1.3
			13	2.81	1.15	1.000	0.4
			5.7	2.28	0.79	1.000	0.7

Figure 3. Time evolution of the diffusivity of DF-1 (A) and AC60 (B) as extrapolated from fitting the experimental data in low and high ionic strength solutions and both 5.7 and 13 nm nanochannels. The table lists the nanochannel diffusivities at $t = 0$ and t = end of experiment as well as the bulk diffusivities as obtained with membranes possessing only the 3 μm microchannels connected to the 200 μm macrochannels (see Methods and Supporting Information). The correlation coefficients and the average percent differences between the experimental data and the fitting curves are also listed.

reservoir at time = 0, and V_{IN} and V_{OUT} are the volumes of the source and sink reservoirs, respectively. The time constant, τ, depends on both D_{EXP} and the equivalent "diffusive resistance", R_{eq}, of the membrane. Details of the calculations of D_{EXP}, including the derivation of R_{eq}, are available in the Supporting Information. Figure 3 depicts the $D_{EXP}(t)$ curves calculated for DF-1 in both nanochannel sizes in I_L and I_H solutions over the full length of the experiment with the table listing the calculated values. For I_H solutions $D_{EXP}(t)$ changes very little from the beginning to the end of the experiment even as the nanochannel cross sections shrink. This is in agreement with the notion that the EDLs are not yet overlapping and negative charge screening is still sufficient to allow for a low energy diffusive pathway through the nanochannel. For I_L solutions, however, the $D_{EXP}(t)$ values fall exponentially with time, a result that is consistent with an increasing potential energy barrier resulting from electrostatic repulsion of the DF-1 by the nanochannels.

***Near-Surface* Diffusion of Positively Charged AC60.** AC60 (MW = 2287 Da) is a hygroscopic fullerene derivative, which in its minimized structure presents a sphere-like conformation of approximately 1.9 nm in diameter.[20] AC60's 12 amino surface residues lead to a net positive charge of $+8.4e$ in I_L solutions at pH 4.25. Unlike the negatively charged DF-1, the positive valence causes AC60 to experience an attractive electrostatic force with respect to the wall surface charge. The extent of the resulting accumulation, including the thickness of the layer near the nanochannel wall, strongly depends on the I that governs both the level of charge shielding and the electrical potential distribution within the nanochannel (λ_D). While highly overlapped EDLs can accumulate charge throughout the nanochannel cross section, nonoverlapping EDLs ($\kappa h \geq 4$) accumulate AC60 in close proximity to the wall surface. Figure 4 schematically depicts the $\psi(z)$ and $n(z)$ that span the cross section for the positively charged AC60 in I_H solutions for both the 13 and 5.7 nm nanochannels. In these I_H solutions, approximately 90% of AC60 diffuses within a 2 nm layer adjacent to the nanochannel walls. The calculated number concentration within this accumulation layer exceeds the source solution concentration in both nanochannel sizes by approximately 1 order of magnitude, with the layer thickness remaining unchanged after the smaller ions, Na^+, Cl^-, HCO_3^-, and CO_3^{2-}, have equilibrated at t = Eq. This

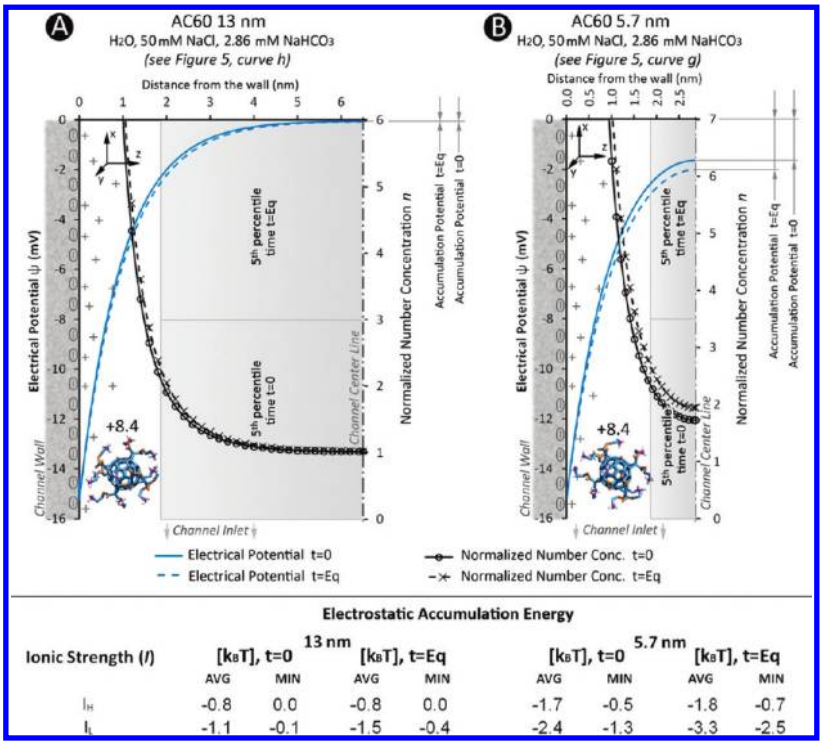

Electrostatic Accumulation Energy

Ionic Strength (*I*)	13 nm [k_BT], t=0 AVG	13 nm [k_BT], t=0 MIN	13 nm [k_BT], t=Eq AVG	13 nm [k_BT], t=Eq MIN	5.7 nm [k_BT], t=0 AVG	5.7 nm [k_BT], t=0 MIN	5.7 nm [k_BT], t=Eq AVG	5.7 nm [k_BT], t=Eq MIN
I_H	-0.8	0.0	-0.8	0.0	-1.7	-0.5	-1.8	-0.7
I_L	-1.1	-0.1	-1.5	-0.4	-2.4	-1.3	-3.3	-2.5

Figure 4. Schematic representations of the electrical potential, $\psi(z)$, and number concentration, $n(z)$, profiles as well as the effective cross sections at times $t = 0$ and $t =$ Eq for AC60 in I_H solutions in both 13 (A) and 5.7 (B) nm nanochannels. For symmetry reasons, the panels show only half of the nanochannel cross section. The time $t =$ Eq represents the establishment of a quasi-equilibrium whereby the concentrations of all other ionic species (Na^+, Cl^-, HCO_3^-, and CO_3^{2-}) except the ionized AC60 have reached a steady state between the source and sink solutions with respect to AC60. $n(z)$ has been normalized with respect to the source solution concentration. The surface charge density on the nanochannel wall was measured to be -1 μC/cm^2. The depletion regions (lighter gray areas) represent the portion of the channel cross section that is occupied by the 5%ile of the $n(z)$ distribution at both time points. The increase of the accumulation energy, E_A, at equilibration resulting from electrostatic attraction of the ionized $AC60^{8.4+}$ by the negative surface charge is also shown to the right side of each panel. The values of E_A are listed in the table. The calculations for all values can be found in Methods and the Supporting Information.

accumulation effect manifests itself as an apparent nanochannel size independent of the release rate, at least in the range from 5.7 to 13 nm, in which the accumulated AC60 comprises a significant fraction of the total quantity of AC60 within the nanochannel. The experimental release data, shown in Figure 5, confirm this observation with statistically equivalent cumulative release profiles of AC60 through both 13 and 5.7 nm nanochannels (curves *g* and *h*).

Similar results were obtained with I_L AC60 solutions in both nanochannel sizes, in which no statistically significant difference is observed between the two release rate profiles (see Figure 5, curves *e* and *f*). The homogenization of the ionic strength within the system, however, causes a significant variation in the $\psi(z)$ and $n(z)$ profiles (see Supporting Information).

Although the variation in $\psi(z)$ and $n(z)$ is substantially larger when compared to I_H AC60 solutions, the accumulation zone at $t = 0$ and $t =$ Eq is still contained within a 2 nm distance from the wall in both 5.7 and 13 nm nanochannels, which explains the similarity between curves *e* and *f*. In this case however, the nanochannel presents a larger electrostatic accumulation

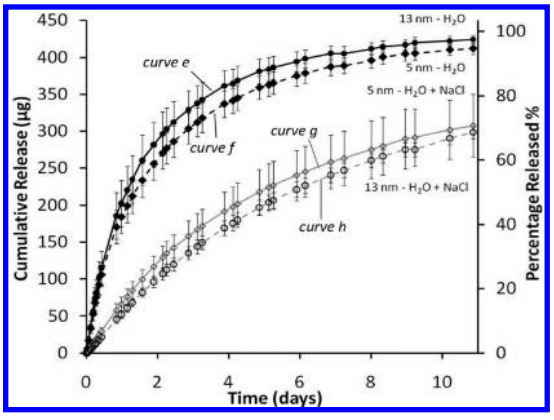

Figure 5. Cumulative released amount and percentage release of AC60 in I_H and I_L solutions in 5.7 and 13 nm nanochannels.

energy, E_A (as compared to I_H AC60 solutions), which drives the accumulation of AC60 to exceed the source solution concentration by a factor of 20. The E_A values are listed in the table in Figure 4.

The accumulation effect is expected to gradually disappear with increased nanochannel height as the average normalized number concentration

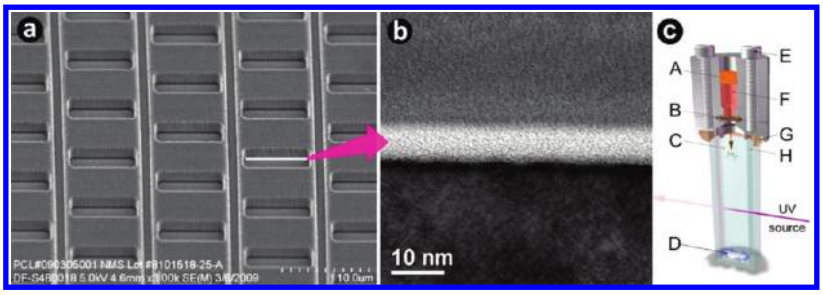

Figure 6. (a) SEM image of the array of outlet microchannels. (b) TEM image of 5.7 nm nanochannel cross section. (c) Schematic of the diffusion testing apparatus: [A] silicone rubber cap, [B] silicon nanochannel membrane, [C] sink solution reservoir, [D] magnetic stir bar, [E] SS316L stainless steel screws, [F] fullerene source solution reservoir, [G] epoxy resin, [H] UV cuvette.

approaches the source concentration. Although the same quantity of accumulated AC60 persists, it constitutes a diminishing fraction of the total number of particles within the nanochannel.

Equation 2 was used to determine D_{EXP} for AC60 in 5.7 and 13 nm nanochannels as described above. The results are shown and tabulated in Figure 3. Once again, the D_{EXP} for the high ionic strength solutions changes very little between $t = 0$ and $t =$ Eq. For the low ionic strength solutions, the D_{EXP} values fall exponentially with time in a similar fashion to the DF-1 results. This would also indicate an accumulation potential that increases with decreasing ionic strength. The primary difference between the release rates for AC60 as opposed to DF-1 is therefore related to the nature of their electrostatic interaction with the nanochannel surface charge. Because DF-1 is repulsed from the nanochannel, a lower ionic strength leads to a higher energy barrier, a lower diffusivity, and a lower concentration of DF-1 in the nanochannel at steady state, all of which reinforce a diminishing release rate. For AC60, reducing the ionic strength also increases the accumulation potential and reduces the effective diffusivity. In this case, however, the AC60 concentration simultaneously increases in a manner that is proportional to the increasing accumulation potential. As such, the release rate does not suffer from the same significant reduction and becomes independent of nanochannel size. Details of the calculations of D_{EXP} for AC60 are available in the Supporting Information.

CONCLUSION

In conclusion, we have demonstrated for the first time the long-term, controlled, release of dendritic-fullerene-1 and amino-fullerene nanoparticles through monodispersed 5.7 and 13 nm nanochannels by exploiting electrostatic *gating* and *accumulation* effects on the diffusive transport of these negatively and positively charged species. In this context, we have elucidated the coupled effects of ionic strength and nanochannel size for purposes of modulating the nanoparticle release profile. Additionally, we have experimentally and theoretically demonstrated the *near-surface* diffusion of the positively charged AC60, which in our range of observation is fully independent of the nanochannel size. Additional contributions from our work include the quantification of the effective diffusivity of these fullerene derivatives at the microscale and in nanoconfinement. A theoretical analysis of the influence of physical and electrostatic confinement on limitations to the degrees of freedom and diffusivity of nanoparticles[27] will be the subject of subsequent investigations. Our findings, obtained with the use of highly charged carriers to eliminate adsorption and aggregation issues, are likely to be applicable to the controlled release of charged drug molecules as well as to a large number of nanovectors[35−40] and thus represent a significant step toward the achievement of metronomically targeted delivery.

METHODS

Due to space constraints only basic information related to the experimental and theoretical methods is included. Detailed descriptions are available in the Supporting Information.

Nanofluidic Membrane. Robust nanofluidic membranes were microfabricated by means of a sacrificial layer technique using silicon-on-insulator (SOI) substrates in two configurations. Densely packed slit nanochannels 5.7 or 13 nm in height (width = 3 μm, length = 1 μm in configuration 1, width = 3 μm, length = 3 μm in configuration 2) and parallel to the membrane surface were produced on top of the SOI device layer using a patterned sacrificial material embedded in deposited silicon nitride. The nanochannels are perpendicularly interfaced to the ambient by inlet channels etched through the SOI device layer and handle wafer and outlet channels etched through the silicon nitride. The membrane structure and microfabrication process are detailed in the Supporting Information and elsewhere.[10]

Membrane Characterization. The nanochannel heights, 5.7 and 13 nm, were verified by observing device cross sections using tunneling and scanning electron microscopy (TEM and SEM); see Figure 6. The root-mean-square roughness of both the silicon and silicon nitride surfaces in the nanochannels was measured by atomic force microscopy and found to be 0.35 and 0.15 nm, respectively. Convective nitrogen gas flow was used to determine membrane uniformity.[41] See Supporting Information for details of the membrane characterization.

Experimental Apparatus. Fullerene release was measured using a custom diffusion testing apparatus comprised of an upstream 300 μL source reservoir and a downstream 4.45 mL sink reservoir separated by the membrane (see Figure 6c). A UV macrocuvette epoxied to one end of the membrane housing comprises the sink reservoir and allows for the measurement of released DF-1 or AC60 by UV absorbance (see Supporting Information).

Experimental Procedure. Separate solutions were prepared by dissolving DF-1 fullerene powder (ChemPacific, Baltimore, MD, USA) in pure Millipore DI water and in a 50 mM NaCl solution to a final concentration of 3 mg/mL. The solutions were then adjusted to pH 7.4 by adding 11 mM sodium carbonate (Na_2CO_3) buffer and sonicated for 10 min to ensure complete DF-1 dissolution. AC60 fullerene derivative was synthesized in Dr. Wilson's laboratory by following the procedure briefly described in the Supporting Information and detailed elsewhere.[42,43] The AC60 solutions were prepared by dissolving 15 mg of AC60 alone or AC60 plus 14.61 mg of NaCl (Fisher, biological grade) in Millipore DI water and adjusting the pH to 4.25 by gradual addition of 10%$_{w/w}$ $NaHCO_3$ solution (corresponding to 1.2 mg of $NaHCO_3$). The volume of solutions was adjusted to 5 mL, at room temperature, by using a volumetric flask, reaching the desired AC60 concentration of 3 mg/mL. Piranha-cleaned (30%:70% H_2O_2/H_2SO_4, v/v) membranes were wetted in 2-propanol for 1 h, then soaked in Millipore DI water for 3 h, and finally immersed in the prepared solutions for 12 h prior to diffusion testing. To assemble the diffusion testing apparatus, the sink reservoir was filled with either Millipore DI water or 50 mM NaCl Millipore DI water solution, the wetted membrane was clamped between the reservoirs, and the source reservoir was filled with 150 μL of the matching DF-1 or AC60 solutions. A silicon rubber plug was used to cap the source reservoir, which was temporarily pierced by a venting needle during insertion to remove any trapped air. Continuous magnetic stirring using PTFE-coated microstir bars ensured sink solution homogeneity. UV absorbance ($\lambda_{DF\text{-}1}$ = 320 nm, λ_{AC60} = 280 nm) was periodically measured using a Beckman Coulter DU 730 UV/vis spectrophotometer to monitor the increasing concentration of DF-1 in the sink reservoir. Membrane cumulative release was calculated using absorbance *vs* concentration standard curves after data normalization with respect to absorbance at time = 0. Diffusion tests were performed with 3 to 5 replicates for each nanochannel size (5.7 and 13 nm) and DF-1 or AC60 solution (Millipore DI water and 50 mM NaCl), for a total of 33 membranes, at a controlled temperature of 23 $\pm$ 0.2 °C. To determine the bulk diffusivity of DF-1 and AC60, similar diffusion tests were performed with microchannel membranes as described in the Supporting Information. Details of the experimental procedure, including solution preparation, UV-absorption standard curves, validation of the experimental protocol, and data analysis are available in the Supporting Information.

Calculation of the Electrical Potential Profiles. In order to calculate the profile of the electrical potential ψ across the channel, along the *z*-axis, we first obtained the wall potential ψ_0 by considering a surface charge density $\sigma = -1$ μC/cm^2 and by using the Grahame equation:[16]

$$\psi_0 = \frac{\sigma}{\kappa\varepsilon\varepsilon_0} = -15.2 \text{ mV} \quad (2a)$$

where $\kappa = 1/\lambda_D$. The obtained ψ_0 value is compatible with the *z*-potential measurements ($\xi = -5.32 \pm 0.15$ mV) performed on the silica substrate by means of a *z*-potential analyzer (Delsa Nano C, Beckman Coulter, Inc.). Prior to performing the measurement, the silica substrate was processed and oxidized with the same procedure as used in the microfabrication of the membrane channels. To calculate $\psi(z)$, we employed the theoretical model developed by Verwey and Overbeek[44] for overlapped EDL regions, which is based on the classical Gouy–Chapman EDL theory. A complete derivation of the model is available elsewhere.[44] The model was derived for an overlapping EDL field between two infinite planes presenting the same potential. In the case of small electrical potential, when $(e\psi)/(k_BT) < 1$ (in our case 0.59 by considering $\psi = \psi_0 = -15.2$ mV), the Poisson–Boltzmann potential equation can be simplified according to the Debye–Hückel approximation in the classical EDL theory to

$$\frac{d^2\psi}{dz^2} = \kappa^2\psi \quad (3a)$$

By considering the boundary conditions

$$\psi|_{z=0} = \psi_0 \quad (4a)$$

$$\left.\frac{d\psi}{dz}\right|_{z=h/2} = 0 \quad (4b)$$

where *h* is the distance between the two planes (corresponding to the nanometric size of our slit channels), the equation can be analytically solved producing a solution describing the potential distribution in an overlapped EDL region:[16]

$$\psi(z) = \psi_0 \frac{\cosh\left(\kappa\left(\frac{h}{2} - z\right)\right)}{\cosh(\kappa z)} \quad (5)$$

See the Supporting Information for additional details on the derivation of $\psi(z)$. Finally, the number concentration profiles across the channel cross section, $n_-(z)$ for DF-1 and $n_+(z)$ for AC60, were calculated and normalized with respect to the number concentration in the source reservoir n_0 by using the Boltzmann equation:

$$\frac{n_\pm}{n_{\pm 0}}(z) = e^{\mp\left(\frac{ez_i\psi(z)}{k_BT}\right)} \quad (7)$$

In order to evaluate the effective available cross section for the DF-1 and AC60 diffusion, which takes into account the electrostatic interaction between the particle and nanochannel walls, we calculated the portion of cross section corresponding to 90% of the diffusing particle population, identified by the coordinate γ along the *z*-axis.

$$\int_{z=h/2}^{z=y} n_-(z)\,dz = 0.45\int_{z=h/2}^{z=0} n_-(z)\,dz \quad (8a)$$

$$\int_{z=\gamma}^{z=0} n_+(z)\,dz = 0.45\int_{z=h/2}^{z=0} n_+(z)\,dz \quad (8b)$$

Conflict of Interest: The authors A.G., D.F., and M.F. hereby disclose a personal financial interest in NanoMedical Systems, Inc. All other authors declare no competing financial interests.

Acknowledgment. The authors are grateful to Jay L. Conyers, who provided us with the DF-1 for the experimental analysis, and Lee Hudson, Ryan Medema, and Randy Goodall (NanoMedical Systems) for their support in the chip fabrication and characterization. This project has been supported with funds from NASA (NNJ06HE06A and NNX08AW91G), Department of Defense (DODW81XWH-09-1-0212), State of Texas Emerging Technology Fund, NanoMedical Systems (NMS), Alliance of NanoHealth (ANH), and the Welch Foundation (C-0627). Author contributions: A.G. conceived the idea, designed the experiment, and directed the study. A.G., E.Z., and J.G. performed the membrane gas flow characterization, fullerene release experiments, and the analysis of the experimental data. A.G. and D.F. wrote the manuscript and performed the analysis of the fullerene diffusion mechanisms. A.Z. contributed in the analysis of the diffusion mechanisms. Y.M., M.A.C., and D.D. synthesized and characterized the AC60 and DF-1 fullerenes and prepared the solutions. S.H. fabricated the nanochannel membranes. L.J.W. supervised the fullerene synthesis. F.H. contributed in the finalization of the manuscript. M.F. supervised the study.

Supporting Information Available: Membrane fabrication process, structure and characterization, custom testing devices, synthesis and structure of DF-1 and AC60, experimental protocols, validation, and data analysis. Theoretical calculations of Debye length, electrostatic potential, accumulation energy,

energy barrier, and derivation of diffusivities are also reported and detailed. This material is available free of charge *via* the Internet at http://pubs.acs.org.

REFERENCES AND NOTES

1. Siwy, Z.; Kosińska, I. D.; Fuliński, A.; Martin, C. R. Asymmetric Diffusion through Synthetic Nanopores. *Phys. Rev. Lett.* **2005**, *94*, 048102.
2. Karnik, R.; Castelino, K.; Majumdar, A. Field-Effect Control of Protein Transport in a Nanofluidic Transistor Circuit. *Appl. Phys. Lett.* **2006**, *88*, 123114–3.
3. Strychalski, E. A.; Levy, S. L.; Craighead, H. G. Diffusion of DNA in Nanoslits. *Macromolecules* **2008**, *41*, 7716–7721.
4. Service, R. F. Materials and Biology: Nanotechnology Takes Aim at Cancer. *Science* **2005**, *310*, 1132–1134.
5. Hubbell, J. A. Materials Science: Enhancing Drug Function. *Science* **2003**, *300*, 595–596.
6. Gu, F.; Zhang, L.; Teply, B. A.; Mann, N.; Wang, A.; Radovic-Moreno, A. F.; Langer, R.; Farokhzad, O. C. Precise Engineering of Targeted Nanoparticles by Using Self-Assembled Biointegrated Block Copolymers. *Proc. Natl. Acad. Sci. U. S. A.* **2008**, *105*, 2586–2591.
7. Giljohann, D. A.; Seferos, D. S.; Daniel, W. L.; Massich, M. D.; Patel, P. C.; Mirkin, C. A. Gold Nanoparticles for Biology and Medicine. *Angew. Chem., Int. Ed.* **2010**, *49*, 3280–3294.
8. Kerbel, R. S.; Klement, G.; Pritchard, K. I.; Kamen, B. Continuous Low-Dose Anti-Angiogenic/Metronomic Chemotherapy: from the Research Laboratory into the Oncology Clinic. *Ann. Oncol.* **2002**, *13*, 12–15.
9. Pasquier, E.; Kavallaris, M.; Andre, N. Metronomic Chemotherapy: New Rationale for New Directions. *Nat. Rev. Clin. Oncol.* **2010**, *7*, 455–465.
10. Grattoni, A.; Shen, H.; Fine, D.; Ziemys, A.; Gill, J.; Hudson, L.; Hosali, S.; Goodall, R.; Ferrari, M. Nanochannel Technology for Metronomic Delivery of Chemotherapeutics. *Pharm. Res.* **2011**, *28*, 292–300.
11. Martin, F.; Walczak, R.; Boiarski, A.; Cohen, M.; West, T.; Cosentino, C.; Ferrari, M. Tailoring Width of Microfabricated Nanochannels to Solute Size Can Be Used to Control Diffusion Kinetics. *J. Controlled Release* **2005**, *102*, 123–133.
12. Walczak, R.; Boiarski, A.; Cohen, M.; West, T.; Melnik, K.; Shapiro, J.; Sharma, S.; Ferrari, M. Long-Term Biocompatibility of Nanogate Drug Delivery Implant. *NanoBioTechnology* **2005**, *1*, 35–42.
13. Deen, W. M. Hindered Transport of Large Molecules in Liquid-Filled Pores. *AIChE J.* **1987**, *33*, 1409–1425.
14. Ziemys, A.; Grattoni, A.; Fine, D.; Hussain, F.; Ferrari, M. Confinement Effects on Monosaccharides Transport in Silica Nanochannels. *J. Phys. Chem. B* **2010**, *114*, 11117–11126.
15. Sparreboom, W.; Van den Berg, A.; Eijkel, J. C. T. Principles and Applications of Nanofluidic Transport. *Nat. Nanotechnol.* **2009**, *4*, 713–720.
16. Van der Heyden, F. H. J.; Stein, D.; Dekker, C. Streaming Currents in a Single Nanofluidic Channel. *Phys. Rev. Lett.* **2005**, *95*, 116104.
17. Partha, R.; Conyers, J. L. Biomedical Applications of Functionalized Fullerene-Based Nanomaterials. *Int. J. Nanomed.* **2009**, *4*, 261–275.
18. Liang, X.-J.; Meng, H; Wang, Y.; He, H; Meng, J.; Lu, J.; Wang, P. C.; Zhao, Y.; Gao, X.; Sun, B.; *et al*. Metallofullerene Nanoparticles Circumvent Tumor Resistance to Cisplatin by Reactivating Endocytosis. *Proc. Natl. Acad. Sci. U. S. A.* **2010**, *107*, 7449–7454.
19. Bakry, R.; Vallant, R. M.; Najam-ul-Haq, M.; Rainer, M.; Szabo, Z.; Huck, C. W.; Bonn, G. K. Medicinal Applications of Fullerenes. *Int. J. Nanomed.* **2007**, *2*, 639–649.
20. Sitharaman, B.; Zakharian, T.; Saraf, A.; Misra, P.; Ashcroft, J.; Pan, S.; Pham, Q. P.; Mikos, A. G.; Wilson, L. J.; Engler, D. A. Water-Soluble Fullerene (C_{60}) Derivatives as Nonviral Gene-Delivery Vectors. *Mol. Pharmaceutics* **2011**, *5*, 567–578.
21. Zakharian, T. Y.; Seryshev, A.; Sitharaman, B.; Gilbert, B. E.; Knight, V.; Wilson, L. J. A Fullerene-Paclitaxel Chemotherapeutic: Synthesis, Characterization, and Study of Biological Activity in Tissue Culture. *J. Am. Chem. Soc.* **2005**, *127*, 12508–12509.
22. Ashcroft, J. M.; Tsyboulski, D. A.; Hartman, K. B.; Zakharian, T. Y.; Marks, J. W.; Weisman, R. B.; Rosenblum, M. G.; Wilson, L. J. Fullerene (C_{60}) Immunoconjugates: Interaction of Water-Soluble C_{60} Derivatives with the Murine Anti-gp240 Melanoma Antibody. *Chem. Commun. (Cambridge, U.K.)* **2006**, 3004–3006.
23. Fine, D.; Grattoni, A.; Hosali, S.; Ziemys, A.; De Rosa, E.; Gill, J.; Medema, R.; Hudson, L.; Kojic, M.; Milosevic, M.; *et al*. A Robust Nanofluidic Membrane with Tunable Zero-Order Release for Implantable Dose Specific Drug Delivery. *Lab Chip* **2010**, *10*, 3074.
24. Grattoni, A.; Gill, J.; Zabre, E.; Fine, D.; Hussain, F.; Ferrari, M. Device for Rapid and Agile Measurement of Diffusivity in Micro- and Nanochannels. *Anal. Chem.* **2011**, *83*, 3096–3103.
25. Sparreboom, W.; Van den Berg, A.; Eijkel, J. C. T. Transport in Nanofluidic Systems: A Review of Theory and Applications. *New J. Phys.* **2010**, *12*, 015004.
26. Brettreich, M.; Hirsch, A. A Highly Water-Soluble Dendro [60] Fullerene. *Tetrahedron Lett.* **1998**, *39*, 2731–2734.
27. Rapuano; Carmona-Ribeiro Physical Adsorption of Bilayer Membranes on Silica. *J. Colloid Interface Sci.* **1997**, *193*, 104–111.
28. Schoch, R. B.; Bertsch, A.; Renaud, P. pH-Controlled Diffusion of Proteins with Different pI Values across a Nanochannel on a Chip. *Nano Lett* **2006**, *6*, 543–547.
29. Cussler, E. L. *Diffusion: Mass Transfer in Fluid Systems*, 2nd ed.; Cambridge University Press, 1997.
30. Bohn, P. W. Nanoscale Control and Manipulation of Molecular Transport in Chemical Analysis. *Annu. Rev. Anal. Chem.* **2009**, *2*, 279–296.
31. Peer, D.; Karp, J. M.; Hong, S.; Farokhzad, O. C.; Margalit, R.; Langer, R. Nanocarriers as an Emerging Platform for Cancer Therapy. *Nat. Nanotechnol.* **2007**, *2*, 751–760.
32. Fu, J.; Schoch, R. B.; Stevens, A. L.; Tannenbaum, S. R.; Han, J. A Patterned Anisotropic Nanofluidic Sieving Structure for Continuous-Flow Separation of DNA and Proteins. *Nat. Nanotechnol.* **2007**, *2*, 121–128.
33. Li, X.; Shantz, D. F. Specific Ion Effects on Nanoparticle Stability and Organocation−Particle Interactions in Tetraalkylammonium−Silica Mixtures. *Langmuir* **2011**, *26*, 18459–18467.
34. Cosentino, C.; Amato, F.; Walczak, R.; Boiarski, A.; Ferrari, M. Dynamic Model of Biomolecular Diffusion through Two-Dimensional Nanochannels. *J. Phys. Chem. B* **2005**, *109*, 7358–7364.
35. Torchilin, V. P. Recent Advances with Liposomes as Pharmaceutical Carriers. *Nat. Rev. Drug Discovery* **2005**, *4*, 145–160.
36. Sutton, D.; Nasongkla, N.; Blanco, E.; Gao, J. Functionalized Micellar Systems for Cancer Targeted Drug Delivery. *Pharm. Res.* **2007**, *24*, 1029–1046.
37. Khemtong, C.; Kessinger, C. W.; Ren, J.; Bey, E. A.; Yang, S.-G.; Guthi, J. S.; Boothman, D. A.; Sherry, A. D.; Gao, J. In vivo Off-Resonance Saturation Magnetic Resonance Imaging of $\alpha v\beta 3$-Targeted Superparamagnetic Nanoparticles. *Cancer Res.* **2009**, *69*, 1651–1658.
38. Partha, R.; Mitchell, L. R.; Lyon, J. L.; Joshi, P. P.; Conyers, J. L. Buckysomes: Fullerene-Based Nanocarriers for Hydrophobic Molecule Delivery. *ACS Nano* **2008**, *2*, 1950–1958.
39. Hanahan, D.; Bergers, G.; Bergsland, E. Less Is More, Regularly: Metronomic Dosing Of Cytotoxic Drugs Can Target Tumor Angiogenesis in Mice. *J. Clin. Invest.* **2000**, *105*, 1045–1047.
40. Davis, M. E.; Zuckerman, J. E.; Choi, C. H. J.; Seligson, D.; Tolcher, A.; Alabi, C. A.; Yen, Y.; Heidel, J. D.; Ribas, A. Evidence of RNAi in Humans from Systemically Administered siRNA *via* Targeted Nanoparticles. *Nature* **2010**, *464*, 1067–1070.
41. Grattoni, A.; De Rosa, E.; Ferrati, S.; Wang, Z.; Gianesini, A.; Liu, X.; Hussain, F.; Goodall, R.; Ferrari, M. Analysis of a Nanochanneled Membrane Structure through Convective Gas Flow. *J. Micromech. Microeng.* **2009**, *19*, 115018.

42. Lee, I.; Mackeyev, Y.; Cho, M.; Li, D.; Kim, J.-H.; Wilson, L. J.; Alvarez, P. J. J. Photochemical and Antimicrobial Properties of Novel C_{60} Derivatives in Aqueous Systems. *Environ. Sci. Technol.* **2009**, *43*, 6604–6610.
43. Chronakis, N.; Hartnagel, U.; Braun, M.; Hirsch, A. A Chiral Dumbbell Shaped Bis(Fullerene) Oligoelectrolyte. *Chem. Commun. (Cambridge, U.K.)* **2007**, 607–609.
44. Verwey, E. J. W.; Overbeek, J. T. G. *Theory of Stability of Lyophobic Colloids*; Elsevier Publishing Company, Inc.: New York, 1948.